**Proceedings of the ASME 2024**
**International Mechanical Engineering Congress and Exposition**
**IMECE2024**
**November 17-21, 2024, Portland, Oregon**

**IMECE2024-145515**

# FLUID-STRUCTURE INTERACTION ANALYSIS OF METACHRONAL PROPULSION AT INTERMEDIATE REYNOLDS NUMBERS

Zhipeng Lou[1], Menglong Lei[1], Margaret L. Byron[2], Chengyu Li[1]

[1] *Case Western Reserve University, Cleveland, OH 44106, USA*

[2] *Pennsylvania State University, University Park, PA 16802, USA*

## ABSTRACT

*Ctenophores swim using flexible rows of appendages called ctenes that form the metachronal paddling. To generate propulsion, each appendage operates a power stroke that strokes backward, followed by a recovery stroke that allows the appendage to readjust its position. Notably, strokes of most metachronal swimmers are asymmetric, with faster power strokes while slower recovery strokes. Previously, the material properties are assumed as isotropic. So, the faster power stoke will lead to more pronounce deformation and the slower recovery stroke will lead to less deformation. However, this contradicts with the observations that power-stroking ctenes have the least deformation and recover deforms more, indicating an anisotropic material behavior. Such anisotropic material is hard to be manufactured, but the anisotropic behavior may be achieved by making the initial structural shape curved. The pre-curved ctene, that bending towards downstream, will be straighten in power stoke while easy to bend during recovery stroke. Our study aims to demonstrate the feasibility of using pre-curved shapes to achieve anisotropic material properties during metachronal swimming. Treating it as fluid-structure interaction (FSI) problem, we integrate our in-house computational fluid dynamics (CFD) solver with a finite element method (FEM) solver, utilizing strong coupling methods for convergence. By comparing the performance of pre-curved ctenes with straight ones, which represent isotropic material properties, we found that the curved ctenes exhibited 26.05% to 65.69% higher cycle-averaged thrust compared to the straight one as stiffness is lower. However, as stiffness increased, the pre-curved ctenes produced 3.92% to 30.58% less thrust than the straight ones. Similar trends were observed in propulsive efficiency, with the pre-curved ctenes demonstrating 46.97% better efficiency at the lowest stiffness but dropping to 34.02% less efficient as stiffness rise. Thus, while the pre-curved initial shape led to better performance at lower stiffness, exceeding a certain stiffness threshold resulted in worse performance compared to straight ctenes. The thrust enhancement from pre-curve shape is due to the drag reduction during recovery stroke, where the curved shape mitigate part of force to point more downward.*

## NOMENCLATURE

| | |
|---|---|
| $F_T$ | Thrust force |
| $C_T$ | Thrust coefficient |
| $C_{PW}$ | Power coefficient |
| $\bar{U}_{tip}$ | Cycle-averaged ctenes tip speed |
| L | Ctene length |
| $f$ | Flapping frequency |
| $Re$ | Reynolds number |
| $u_i$ | Velocity component |
| $P$ | Pressure |
| $\nu$ | Seawater kinematic viscosity |
| T | Period |
| K | Reduced stiffness |

## 1. INTRODUCTION

Metachronal paddling is a commonly adopted swimming technique for small organisms equipped with multiple swimming appendages such as cilia, pleopods, or other structures like those found in ctenophores, copepods, and krill [1–6]. During the metachronal swimming, each closely spaced appendage undergoes a power stroke opposite to the direction of swimming motion, followed by a recovery stroke to readjust its position. The power stroke generates thrust, while the recovery stroke encounters drag force. To ensure efficient collaboration without interference between adjacent appendages, each typically strokes with a certain phase lag against its neighbor [7,8]. For optimal performance and to mitigate interference, these organisms have evolved flexible appendages that can deform dynamically to facilitate the swimming performance [9,10]. Moreover, many species adopt temporal asymmetrical strokes where the power stroke is faster than the recovery stroke to maximize thrust and minimize drag [11,12].

As the material of appendages are usually assumed as isotropic, where the stiffness remains the same when the appendage stroke in either direction. Based on this assumption, the deformation in power stroke will be more pronounced due to higher acceleration, comparing to less deformation in recovery stroke due to gentler acceleration. However, the observation of animals, like ctenophores, contradicts this assumption, showing that the deformation in power stroke is smaller than in recovery stroke [11,12]. Thus, the ctenes of ctenophore is stiffer in the power stroke than the recovery stroke, indicating anisotropic material behavior.

For natural ctenophores, the anisotropic material of ctenes may be controlled through adjusting the ATP supply to the ctenes [13,14]. However, replicating this control in engineering designs presents significant technical challenges. An alternative approach is to utilize isotropic materials while mimicking distinct deformations in opposite directions. For example, researchers have designed soft robotic appendages for jellyfish robots, reinforcing one surface to prevent bending on one side while allowing bending on the other [15]. To realize stiffer material property in power stroke and softer material property in recovery stroke, each ctene can be originally made with curvature and bended against swimming direction, making the bending harder in power stroke while easier in recovery stroke due to such initial structural shape.

Our study aims to demonstrate the feasibility of using pre-curved shapes to achieve anisotropic material properties during metachronal swimming. To address this, we treat the problem as a fluid-structure interaction (FSI) problem and integrate our in-house computational fluid dynamics (CFD) solver with a finite element method (FEM) solver, utilizing strong coupling methods for convergence. By comparing the performance of pre-curved ctenes with straight ones, which represent isotropic material properties, we aim to investigate the influence of the initial structural shape on metachronal paddling. The insights gained from this study will offer valuable guidance for engineering designs inspired by metachronal swimming animals, potentially leading to advancements in the development of biomimetic swimming robots and propulsion systems.

## 2. METHODOLOGY

### 2.1 Kinematics

This study employs two types of 2D flexible ctenes with the same length ($L$). One type of ctene is entirely straight, referred to as the straight ctene (figure 1a), while the other is initially bent into a 60-degree arc while maintaining the ctene length as $L$, referred as the curved plate (figure 1b). To mimic the metachronal paddling, five ctenes of each type are placed in a row and rooted on a straight substrate with uniform spacing of L. The ctene roots are given sinusoidal stroke motion as equation (1).

$$\alpha = A_\alpha \sin(2\pi f t) \tag{1}$$

where the $\alpha$ is the pitch angle, $A_\alpha$ is the amplitude, and $f$ is the normalized beating frequency. In this study, the amplitude $A_\alpha$ is 60° and normalized frequency $f$ is 1. Figure 1c shows the time history of the pitch angle of two types of plates. To prevent contact with the substrate, the pitch angle of curved ctenes is shifted up by 15° while maintaining the same amplitude.

At the beginning of the stroke period, the leftmost straight ctene starts with a pitch angle of 60°, whereas in the curved case, it begins at 75°. Subsequently, the adjacent ctenes in both cases exhibit a phase lag of $0.25T$ relative to the first one. This phase lag remains consistent for all subsequent ctenes, maintaining the same relative timing with respect to the preceding ctenes.

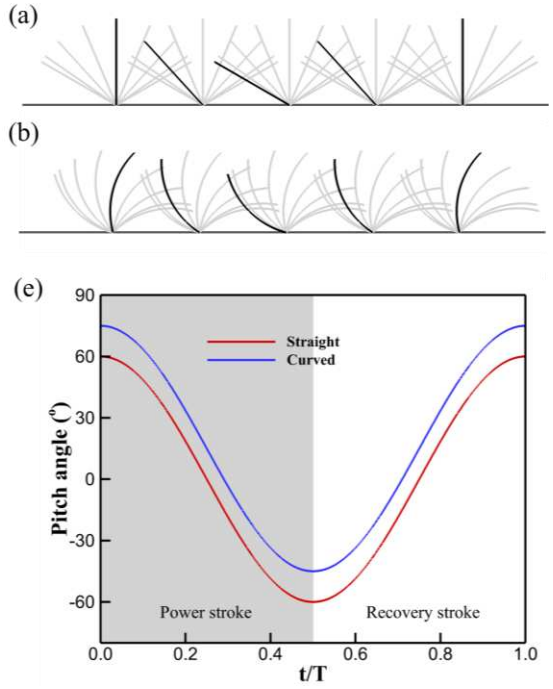


Figure 1. A row of (a) straight and (b) curved ctene models rooted on the substrate with prescribed motion. The black line illustrates ctenes with a pitch angle of zero, while the grey line depicts ctenes at eight evenly spaced time intervals during one cycle. (c) Time history of the prescribed pitch angle for the first ctene of straight and curved model. The pitch angles of the two models have a constant difference of 15°.

## 2.2 Governing equations and numerical method for the flow

The governing equations adopted here are the unsteady incompressible viscous Navier-Stokes equations, which are shown in equation (2) and (3), and discretized using the collocated grid arrangement, where the primitive variables ($u_i$ and $p$) are stored in the cell center.

$$\frac{\partial u_i}{\partial x_i} = 0 \tag{2}$$

$$\frac{\partial u_i}{\partial t} + \frac{\partial (u_i u_j)}{\partial x_j} = -\frac{1}{\rho}\frac{\partial p}{\partial x_i} + \nu \frac{\partial}{\partial x_j}\left(\frac{\partial u_i}{\partial x_j}\right) \tag{3}$$

where $u_i$ (for i = 1,2,3) denotes the velocity components in the x, y, and z directions respectively. $p$ is the normalized pressure, $\nu$ is the kinematics velocity, and $\rho$ is the fluid density.

The above equations are solved by a finite difference-based immersed-boundary method in a non-body-conforming Cartesian grid, which are integrated in time using the fractional step method. The advantage of the immersed-boundary method is that it is not necessary to use complicated re-meshing algorithms that are used by other conventional body conformal methods. This flow solver has been successfully applied to studies of biological propulsion [16–19]. Details of the CFD solver in solving the Navier–Stokes equations are elaborated and validated in our previous studies [20–23].

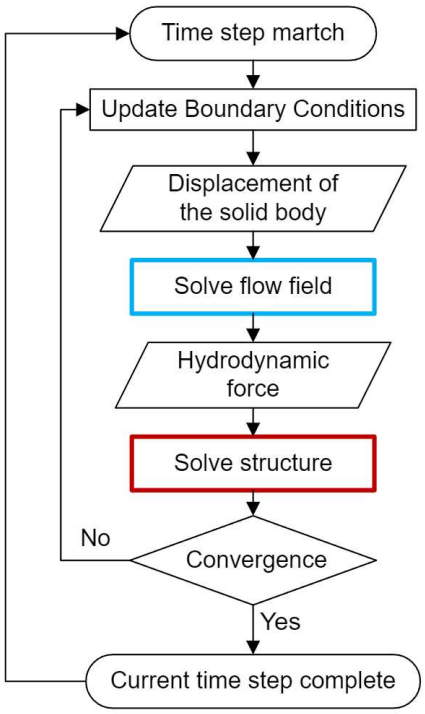


Figure 2. The definition of the width W and length L of the model.

### 2.2.1 Fluid structure interaction solver

To solve the fluid structure interaction problem, this study integrated our in-house computation fluid dynamic (CFD) solver with a finite element method (FEM) solver (Vega FEM, University of Southern California, Los Angeles, CA) [24]. At each time step, the CFD solver is strongly coupled with the FEM solver, as shown in Figure 2. Similar coupling methods have been successfully adopted by studies for fish swimming and insect flight [25].

## 2.3 Simulation setup

The flow domain is discretized into a non-uniform Cartesian grid which has the dimension of 30L×5L (figure 3a), where the total grid size is 0.26 million. To balance the computational cost and quality, two-layer mesh with different mesh density is used. A dense layer is placed closely round the model. Outside, a less dense mesh layer wraps the denser mesh region. The far field is relatively coarse but can provide smooth transition to the flow boundary. In natural, those beating appendages are rooted on substrates. To mimic ground effect from the substrate, the bottom boundary is non-slip. The rest of the boundaries are set to zero-gradient boundary conditions.

The mesh in the FEM solver is illustrated in figure 3b for the straight plate and in figure 3c for the curved plate, where the shapes in two cases represent the initial state of the models. The averaged thickness $\bar{h}$ is 0.0375L.

In all the simulations, the Reynolds number ($\mathrm{Re} = \bar{U}_{\mathrm{tip}}\mathrm{L}/\nu$) is 50. The Poisson's ratio ($v_s$) is 0.25. The mass ratio ($m^* = \rho_s \bar{h}/\rho_f L$) is 0.375. Multiple reduced stiffness ($K = E\bar{h}^3/12\rho_f \bar{U}_{tip}{}^2 L^3$) has been tested, including 0.05, 0.11, 0.24, 0.52, and 1.11.

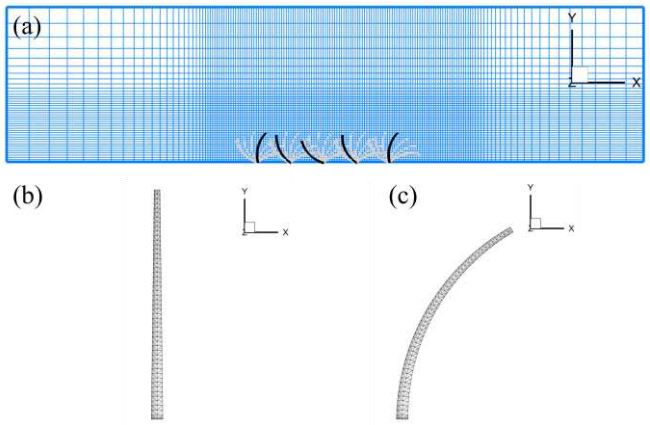


**Figure 3.** (a) The computational grids for all simulations (side view). The mesh for (b) straight plate case and (c) curved plate case.

## 2.4 Evaluation of hydrodynamic performance and nondimensionalization

By solving the Navier-Stokes equations, the surface pressure and the shear stress are computed, which are used to calculate the hydrodynamic forces on each ctene. To evaluate the overall hydrodynamic performance, we calculated the individual ctene thrust coefficients $C_T$ which is derived from the vertical component, thrust $F_T$, given by equation (4),

$$C_T = \frac{F_T}{\frac{1}{2}\rho_f \bar{U}_{tip}^2 s} \quad (4)$$

where $\rho_f$ is the fluid density, $\bar{U}_{tip}$ is the cycle-averaged tip velocity, and $s$ is the surface area of the plates.

The hydrodynamic power is calculated as the surface integral of the product of the pressure and velocity at each surface element, which is defined by equation (5). The power coefficient is given by equation (6).

$$P = -\iint (\Delta p + \Delta\tau)\boldsymbol{n} \cdot \boldsymbol{u_c}\, ds \quad (5)$$

$$C_{pw} = \frac{P}{\frac{1}{2}\rho_f \bar{U}_{tip}^2 s} \quad (6)$$

where $\Delta p$ and $\Delta\tau$ are the pressure difference and shear stress difference across the plate, $\boldsymbol{n}$ is unit normal vector of an element of the plates, $\boldsymbol{u_c}$ is the cell-centered velocity vector of the element, $ds$ is the area of the element.

## 3. VALIDATION

We conducted the validation by comparing the results of our solver with the results from Dai et al and Liu et al [26,27]. In the validation, a 3D flat plate was given a rotational motion along its leading edge, where the pitch angle $\alpha$ is defined in figure 4. The rotational kinematics is given by the equation (1) and the heaving amplitude $\alpha_0$ is 12°.

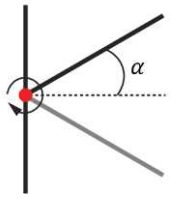


**Figure 4.** The definition of the kinematics and pitch angle $\alpha$ from side view in the validation cases

To validate our solver, 5 simulations have been conducted under different reduced stiffness K of 0.1, 0.5, 1, 2, 5, and 50. The trailing edge amplitude A that normalized by the length L is calculated for different K, as defined in figure 5(b). The results of our simulation are shown in figure 5(a) which are also compare with the ones from the other two studies. Our results show good alignment with the other two studies.

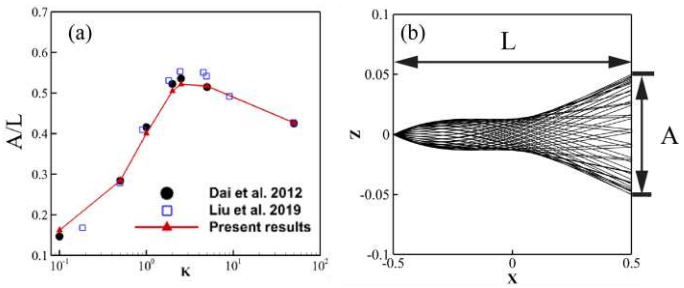


**Figure 5.** (a)The comparison between the results from our solver and other studies, (b)The definition of the trailing edge amplitude.

## 4. RESULTS AND DISCUSSIONS

Figure 6 presents the resulting deformation of the plates of different values of reduced stiffness K. During recovery stroke, the curved plates have larger curvature and lower tip position than the straight case under the same K. This may reduce the drag force during the recovery stroke due to lower cross section area against incoming flow []. During the power stroke, the curved plates is straighter than the straight plates. This attributes to that the pre-curved shape of the curved plates cancels out the deformation stemming from the hydrodynamic resistance.

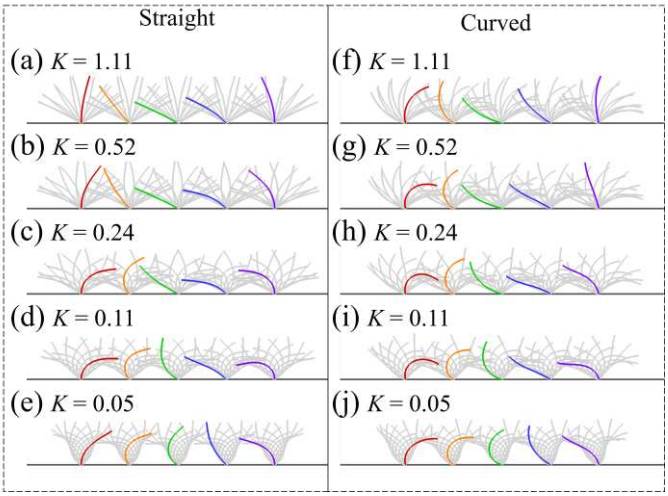


**Figure 6.** (a-f) The resulting deformed straight plates as stiffness from 1.11 to 0.05. (g-n) The resulting deformed curved plates as stiffness from 1.11 to 0.05. The highlighted plates are at t/T = 0.5. The gray trailing shadow of plates represents the deformed plate at every 0.125T.

Figure 7 shows the time history of mean thrust coefficient $C_T$ and mean hydrodynamic power coefficient $C_{pw}$, averaged across five ctenes. These mean coefficients are computed after removing the phase lag in the force history. Across all cases, thrust peaks occur during the midpoint of the power stroke, while reaching a minimum negative value during the midpoint of the recovery stroke. During the power stroke, the peak thrust values for the straight cases across all K values closely resemble those of the curved cases. Conversely, during the recovery stroke, for K values ranging from 0.05 to 0.24, the peak drag of the straight cases is consistently smaller than that of the curved cases, indicating a phenomenon of drag reduction. However, as K increases, up to 1.11, this drags reduction shifts to drag increment. The peak drag experienced by the curved cases during the recovery stroke surpasses that of the straight cases considerably.

In terms of the power consumption, as K ranges from 0.05 to 0.24, the peak power of the curved cases is lower than that of the straight cases. However, as K extends from 0.52 to 1.11, the power of the curved cases during the recovery stroke experiences a significant increase compared to the straight cases.

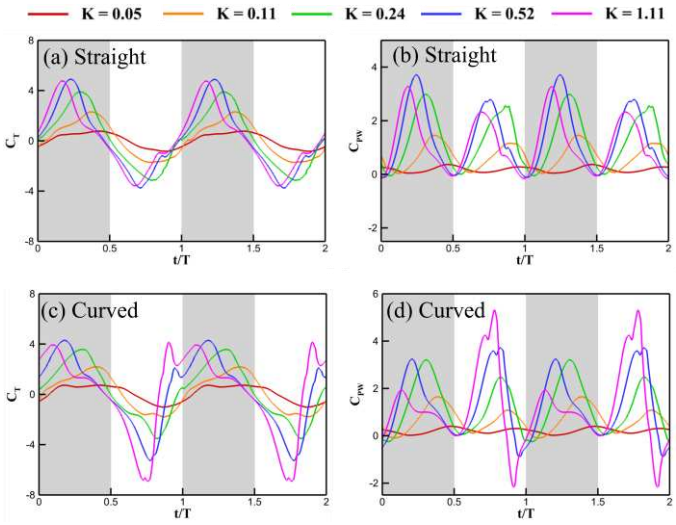


**Figure 7.** (a) The mean thrust coefficient $C_T$ and (b) power coefficient $C_{pw}$ of straight plate row. (c) The thrust coefficient $C_T$ and (d) power coefficient $C_{pw}$ of curved ctene row. Shaded area represents the power stroke period.

For the comparison of the overall performance between two cases, figure 8 shows the cycle-averaged thrust coefficient $C_T$ and thrust to power ratio $C_T/C_{pw}$ at various K. Across the range of K from 0.05 to 0.24, the curved case has higher thrust and propulsive efficiency. The curved ctene row, with $C_T$ from 0.074 to 0.221, demonstrates 65.69% to 26.05% higher thrust than the straight case's 0.045 to 0.175. The $C_T/C_{pw}$ of the curved ctene row ranges from 0.353 to 0.181, which is 46.97% to 32.18% higher than the straight case's 0.240 to 0.137. However, as K increases beyond 0.52 up to 1.11, the curved cases exhibit diminished overall performance. The curved case has $C_T$ of 0.174 to 0.108 which is 3.92% to 30.58% less than straight case's 0.181 to 0.155. Besides, the $C_T/C_{pw}$ of the curved ctene row ranges from 0.129 to 0.089, which is 3.37% to 34.02% lower than the straight case's 0.133 to 0.135. Hence, the pre-curve appendage offers advantages that enhance thrust and propulsive power efficiency at lower stiffness levels, but these benefits transition into negative effects on overall performance as stiffness reaches a critical threshold.

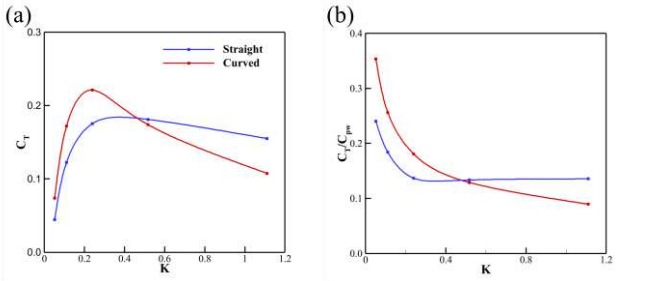


Figure 8. (a) Cycle-averaged thrust coefficient $C_T$ and Cycle-averaged thrust to power ratio $C_T/C_{pw}$ at different reduced stiffness K.

To further investigate the factors driving performance enhancement, we compare the pressure fields of straight and curved cases at a K value of 0.24, which represents the optimal condition for higher thrust and efficiency (figure 9). At either t/T of 0.25 or 0.75, the ctenes during the power stroke phase exhibit similarities between the two cases, consistent with observations from the force history (figure 7a and c). However, notable differences emerge in the pressure fields near the ctenes during the recovery phase, particularly evident around the second to fourth ctenes (as shown in figure 9b and 9d). These disparities result in distinct force directions. Due to the greater curvature, the forces exerted in curved cases point more downward compared to the straight case, resulting in reduced horizontal force components, indicative of less drag force. Consequently, the thrust enhancement stemming from the pre-curved geometry may be primarily attributed to drag reduction resulting from the downward-directed surface force.

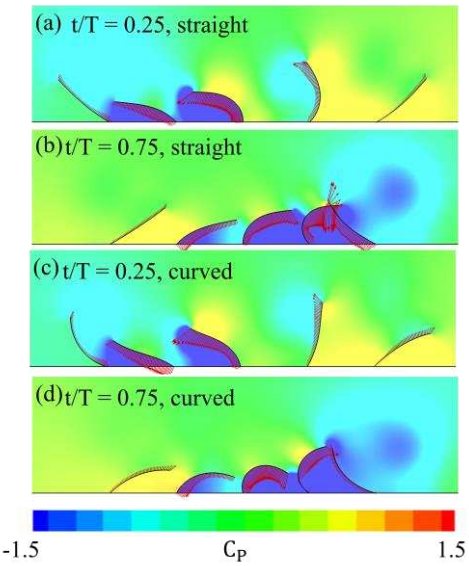


Figure 9. As K = 0.24, contour of pressure coefficient $C_P$ of straight and curved case at t/T = 0.25 and t/T = 0.75.

Furthermore, given that the thrust enhancement become negative effect as ctenes become stiffer, it is crucial to understand the underlying cause of this reversal. Figure 10 illustrates the pressure fields of the two cases at two time

instants with a K value of 1.11. At this stiffness level, the curved case exhibits the poorest performance compared to the straight case. The pressure fields around the ctenes during the power phase, such as the third ctene in Figure 10a and 10c, show similarities between the two cases, consistent with observations at K = 0.24. However, during the recovery stroke, the pressure on the posterior side of the ctenes in the curved case is significantly lower than that in the straight case (second to fourth ctene in Figure 10b and 10d). This finding corroborates previous force history results indicating a dramatic increase in drag force experienced by the curved cases during the recovery stroke

(figure 7a and c). Compared with the straight case, regions of low-pressure during recovery stroke in the curved case behind the ctenes is much strengthen. These strengthened low-pressure zones behind the ctenes may arise from larger curvature of the curved ctenes. The curvature of curve ctenes forms a cup that cause a cupping effect which eventually forms a low-pressure zone behind ctenes, causing more drag.

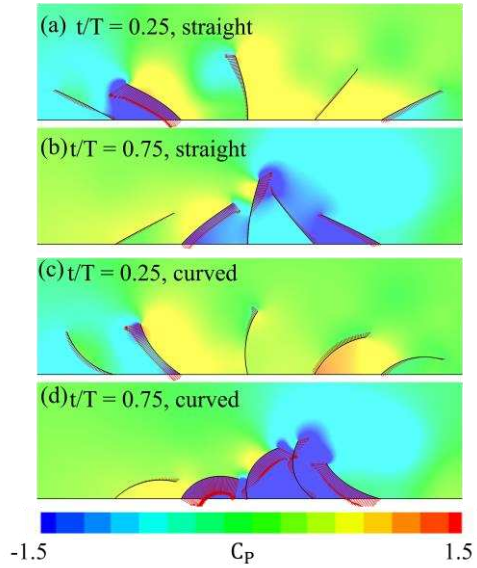


Figure 10. As K = 1.11, contour of pressure coefficient $C_P$ of straight and curved case at t/T = 0.25 and t/T = 0.75.

The drag experienced during the recovery stroke primarily hinges on the pressure gradient between the anterior and posterior surfaces of the ctenes, indicating how much lower the pressure in the low-pressure zone is compared to the anterior pressure. Thus, weakening the intensity of the lower pressure zone could lead to drag reduction. This mechanism operates simultaneously with the previously observed drag reduction resulting from the downward-pointing force direction at lower stiffness levels. When stiffness is low, the low-pressure zone in both cases exhibits similarity, and drag reduction primarily stems from the more pronounced downward force direction. However, as stiffness exceed a certain threshold, the straight case becomes less prone to bending, thereby weakening the previous cupping effect and the associated low-pressure zone. The drag reduction effect resulting from the weakening of the low-pressure zone outweighs that of the downward-pointing force direction. This elucidates why thrust enhancement diminishes as stiffness exceeds a certain threshold. Furthermore, it offers insight for engineering designs, suggesting that pre-curved appendages may reduce drag and enhance performance when the material is less stiff, while the benefits of the pre-curved shape may lead to adverse effects on performance if the material is too stiff.

## 5. CONCLUSIONS

In this study, we have integrated our in-house computational fluid dynamics (CFD) solver with a finite element method (FEM) solver to solve fluid structure interaction (FSI) problems using strong coupling methods. Employing this FSI solver, we compared the hydrodynamic performance of 2D ctenes with initially straight and curved structural shapes. Results of this comparison varied significantly based on stiffness.

At lower stiffness levels (K = 0.05-0.24), the pre-curved ctenes exhibited 26.05% to 65.69% higher cycle-averaged thrust compared to the straight one. However, as stiffness increased, the pre-curved ctenes produced 3.92% to 30.58% less thrust than the straight ones. Similar trends were observed in propulsive efficiency, with the pre-curved ctenes demonstrating 46.97% better efficiency at the lowest stiffness but dropping to 34.02% less efficient at K = 1.11. Thus, while the pre-curved initial shape led to better performance at lower stiffness, exceeding a certain stiffness threshold resulted in worse performance compared to straight ctenes.

In one hand, at lower stiffness, the thrust enhancement stemmed primarily from the curvature of the pre-curved ctenes, which directed the acting force more downward during recovery strokes, leading to drag reduction. On the other hand, at high stiffness, the decline in thrust was attributed to the straight ctenes' reduced ability to form cups, which are more prominent at lower stiffness. This interference weakened the lower-pressure zone posterior to the ctenes during recovery strokes, outweighing the benefits of the pre-curved initial shape and resulting in decreased overall thrust and efficiency.

## 6. ACKNOWLEDGMENTS

This research was supported by the National Science Foundation to C. Li (NSF CBET-2451990) and to M. L. Byron (NSF CBET-2120689).

## REFERENCES

1. Byron ML *et al.* 2021 Metachronal Motion across Scales: Current Challenges and Future Directions. *Integr Comp Biol* **61**, 1674–1688. (doi:10.1093/icb/icab105)

2. Byron M, Santhanakrishnan A, Murphy D. 2021 Metachronal Coordination of Multiple Appendages for Swimming and Pumping. *Integr Comp Biol* **61**, 1561–1566. (doi:10.1093/icb/icab181)

3. Tamm SL. 2014 Cilia and the life of ctenophores. *Invertebrate Biology* **133**, 1–46. (doi:10.1111/ivb.12042)

4. Murphy DW, Webster DR, Kawaguchi S, King R, Yen J. 2011 Metachronal swimming in Antarctic krill: Gait kinematics and system design. *Mar Biol* **158**, 2541–2554. (doi:10.1007/s00227-011-1755-y)

5. Lenz PH, Takagi D, Hartline DK. 2015 Choreographed swimming of copepod nauplii. *J R Soc Interface* **12**. (doi:10.1098/rsif.2015.0776)

6. Van Duren LA, Videler JJ. 2003 Escape from viscosity: the kinematics and hydrodynamics of copepod foraging and escape swimming. *Journal of Experimental Biology* **206**, 269–279. (doi:10.1242/JEB.00079)

7. Ford MP, Lai HK, Samaee M, Santhanakrishnan A. 2019 Hydrodynamics of metachronal paddling: Effects of varying Reynolds number and phase lag. *R Soc Open Sci* **6**. (doi:10.1098/rsos.191387)

8. Ford MP, Santhanakrishnan A. 2021 On the role of phase lag in multi-appendage metachronal swimming of euphausiids. *Bioinspir Biomim* **16**, 066007. (doi:10.1088/1748-3190/ABC930)

9. Hoover AP, Cortez R, Tytell ED, Fauci LJ. 2018 Swimming performance, resonance and shape evolution in heaving flexible panels. *J Fluid Mech* **847**, 386–416. (doi:10.1017/jfm.2018.305)

10. Daniels J, Aoki N, Havassy J, Katija K, Osborn KJ. 2021 Metachronal swimming with flexible legs: a kinematics analysis of the midwater polychaete Tomopteris. *Integr Comp Biol* **61**, 1658–1673. (doi:10.1093/ICB/ICAB059)

11. Herrera-Amaya A, Seber EK, Murphy DW, Patry WL, Knowles TS, Bubel MM, Maas AE, Byron ML. 2021 Spatiotemporal asymmetry in metachronal rowing at intermediate Reynolds numbers. *Integr Comp Biol* **61**, 1579–1593. (doi:10.1093/icb/icab179)

12. Lou Z, Adrian H-A, Byron ML, Li C. 2022 Hydrodynamics of metachronal motion: effects of spatial asymmetry on the flow interaction between adjacent appendages. In *Proceedings of the ASME 2022 Fluids Engineering Division Summer Meeting*,

13. Barlow D, Sleigh MA. 1993 Water Propulsion Speeds and Power Output By Comb Plates of the Ctenophore Pleurobrachia Pileus Under Different Conditions. *Journal of Experimental Biology* **183**, 149–164. (doi:10.1242/jeb.183.1.149)

14. Okamoto K-II, Nakaoka Y. 1994 Reconstitution of metachronal waves in ciliated cortical sheets of Paramecium. II.Asymmetry of the ciliary movements. *Journal of Experimental Biology* **192**, 73–81. (doi:10.1242/jeb.192.1.73)

15. Frame J, Lopez N, Curet O, Engeberg ED. 2018 Thrust force characterization of free-swimming soft robotic jellyfish. *Bioinspir Biomim* **13**. (doi:10.1088/1748-3190/aadcb3)

16. Lou Z, Li C. 2023 Unsteady Aerodynamics and Wake Structures of Butterfly in Forward Flight. (doi:10.2514/6.2023-4241)

17. Lionetti S, Hedrick TL, Li C. 2023 Numerical investigation of olfactory performance in upwind surging hawkmoth flight. (doi:10.2514/6.2023-4242)

18. Lei M, Lou Z, Wang J, Dong H, Li C. 2024 Hydrodynamics of Metachronal Rowing at Intermediate Reynolds Numbers. *ASME International Mechanical Engineering Congress and Exposition, Proceedings (IMECE)* **9**. (doi:10.1115/IMECE2023-112572)

19. Menzer A, Lei M, Li C, Dong H. 2024 A Multiphysics Approach to Understanding Chemoreception in Bio-Robotic Fish Schools. *ASME International Mechanical Engineering Congress and Exposition, Proceedings (IMECE)* **9**. (doi:10.1115/IMECE2023-114543)

20. Li C, Dong H. 2016 Three-dimensional wake topology and propulsive performance of low-aspect-ratio pitching-rolling plates. *Physics of Fluids* **28**. (doi:10.1063/1.4954505)

21. Lionetti S *et al.* 2023 A new propulsion enhancement mechanism in metachronal rowing at intermediate Reynolds numbers. *J Fluid Mech* **974**, A45. (doi:10.1017/JFM.2023.739)

22. Lionetti S, Hedrick TL, Li C. 2022 Aerodynamic explanation of flight speed limits in hawkmoth-like flapping-wing insects. *Phys Rev Fluids* **093104**, 1–24. (doi:10.1103/PhysRevFluids.7.093104)

23. Liu Y, Lozano AD, Hedrick TL, Li C. 2021 Comparison of experimental and numerical studies on the flow structures of hovering hawkmoths. *J Fluids Struct* **107**, 103405. (doi:10.1016/j.jfluidstructs.2021.103405)

24. Sin FS, Schroeder D, Barbič J. 2013 Vega: Non-linear FEM deformable object simulator. *Computer Graphics Forum* **32**, 36–48. (doi:10.1111/j.1467-8659.2012.03230.x)

25. Wang J, Deng X, Lauder G V., Dong H. 2019 Numerical investigation on hydrodynamic performance of flapping plates with non-uniform spanwise flexibility using fluid structure interaction. *AIAA Aviation 2019 Forum* , 1–10. (doi:10.2514/6.2019-3434)

26. Dai H, Luo H, de Sousa PJSAF, Doyle JF. 2012 Thrust performance of a flexible low-aspect-ratio pitching plate. *Physics of Fluids* **24**. (doi:10.1063/1.4764047)

27. Liu G, Geng B, Zheng X, Xue Q, Dong H, Lauder G V. 2019 An image-guided computational approach to inversely determine in vivo material properties and model flow-structure interactions of fish fins. *J Comput Phys* **392**, 578–593. (doi:10.1016/j.jcp.2019.04.062)